Effective Resolution of Phase-contrast Images in X-ray Microscopy

Yoshikazu Yamaguchi[a,*], Ryuichi Shimizu[a], Takashi Ikuta[b], Tetsuo Kikuchi[c], and Sadayuki Takahashi[c]
[a]*Department of Information Science and Technology, Osaka Institute of Technology*
1-79-1 Kitayama, Hirakata, Osaka 573-0196, Japan
[b]*Department of Lightwave Sciences, Osaka Electro-Communication University*
18-8 Hatsu-cho, Neyagawa, Osaka 572-8530, Japan
[c]*X-ray Research Laboratory, Rigaku Corp.*
2-9-12 Matsubara-cho, Akishima, Tokyo 169-8666, Japan
[*]d1d05a02@info.oit.ac.jp

(Received: October 2, 2006 ; Accepted: November 24, 2006)

A simple model for the spatial resolution of phase-contrast images obtained by X-ray microscopy is proposed. In principle, the model is based on Fresnel's diffraction of a point phase object and applied to interpret the X-ray microscopic images of an ant and a bee taken under different experimental conditions.

The source sizes of the X-rays were estimated by Monte Carlo calculation. Using the sizes of the X-ray sources, the spatial resolutions of the phase-contrast images were also estimated according to the proposed model. The results indicate that the present simple model has expressed the high spatial resolution achieved by X-ray microscopy with considerable success, shedding a closer insight into a new world of phase-contrast X-ray microscopy.

1. Introduction

The X-ray microscope has recently been drawing renewed attention for its wider applicability to 3-dimensional tomography, especially for biomedical studies, and commercial products have been under development by manufacturers. Since von Ardenne [1] proposed the use of an electron microprobe for obtaining a small-size X-ray source in the early 1940s, it had long been believed that the spatial resolution of X-ray microscopy is wholly limited by the spot size of X-ray source. In an X-ray microscope, therefore, an electron microprobe of high current density was used to bombard a thin film target so as to make electron diffusion in the target as small as possible.

However, Wilkins *et al.* [2] revealed that a phase-contrast image observed under an X-ray microscope could attain a higher spatial resolution than does a conventional amplitude-contrast (absorption) image. Although they pointed out the potential of phase-contrast images for higher spatial resolution, a more concrete expression of the spatial resolution attained by a phase-contrast X-ray microscope is yet to be explained.

This paper aims at deriving a simple expression for evaluating an effective spatial resolution of the phase-contrast image in X-ray microscopy, enabling realization of an experimental condition for higher spatial resolution. For this, the effective spot size of the X-ray source was evaluated for various experimental conditions by a Monte Carlo (MC) simulation approach, the source program of which we recently wrote in C++ for wider practical use. By applying the approach to X-ray microscopic observations of an ant and a bee under different experimental conditions, it has been confirmed that the present approach achieves the desired experimental results with considerable success.

2. Monte Carlo simulation model

2.1 Scattering processes

The present MC simulation model is based on the uses of the screened Rutherford scattering formula and Bethe's stopping power equation to describe the elastic and inelastic scattering processes of a penetrating electron in a target, respectively. The scattering angle of elastic scattering is

calculated from [3]

$$\frac{\mathrm{d}\sigma_{Rutherford}}{\mathrm{d}\Omega} = \frac{4{m_0}^2 Z^2 e^4}{\hbar^4 (q^2 + a_{scr}^{-2})^2} \quad , \tag{1}$$

where m_0 is the rest mass of the electron, Z the atomic number of the target atom, e the electron charge, and q the scattering vector, $q = |\boldsymbol{q}|$, related to the scattering angle, θ, as

$$q = 2k_0 \sin(\theta/2) \quad , \tag{2}$$

where k_0 is the wavenumber of the penetrating electron. The screening distance a_{scr} is expressed as

$$a_{scr} = \frac{0.885 a_0}{Z^{1/3}} \quad , \tag{3}$$

where a_0 is the Bohr radius.

The energy loss of a penetrating electron along its trajectory is calculated by [4]

$$-\frac{\mathrm{d}E}{\mathrm{d}s} = \frac{2\pi N_A e^4 \rho Z}{m_0 v^2 A_0}\left[\ln\frac{m_0 v^2 E}{2I^2(1-\beta^2)} - (2\sqrt{1-\beta^2} - 1 + \beta^2)\ln 2 + 1 - \beta^2 + \frac{1}{8}(1-\sqrt{1-\beta^2})^2\right], \tag{4}$$

where v is the velocity of the electron, E the kinetic energy of the electron, N_A Avogadro's number, ρ the density of the target material, A_0 the atomic weight, I the mean excitation energy given as [5],

$$I = 9.76Z + 58.5Z^{-0.19} \ [\mathrm{eV}], \tag{5}$$

and β is the relativistic factor.

2.2 Generation of continuous X-rays

The continuous X-rays of photon energy $h\nu$ generated by a penetrating electron are calculated using the Kirkpatrick-Wiedmann-Statham analytical expression, in which the double differential bremsstrahlung cross section with the relativistic correction is expressed as

$$\frac{\mathrm{d}^2\sigma}{\mathrm{d}(h\nu)\mathrm{d}\Omega} = \frac{\sigma_x(1-\cos^2\phi) + \sigma_y(1+\cos^2\phi)}{(1-\beta\cos\phi)^2}. \tag{6}$$

In eq. (6), the x-axis is defined as the velocity vector of the moving electron, ϕ is the emission angle of an X-ray photon with regard to the x-axis, σ_x and σ_y are the x- and y-components of the differential cross section, respectively. X-ray emissions in the y-z plane (i.e., the plane normal to the velocity of the moving electrons) are isotropic. The x-component of the bremsstrahlung cross section is given by Kirkpatrick-Wiedmann as [6]

$$\sigma_x = \frac{0.252 + a(Q-0.135) - b(Q-0.135)^2}{Uh\nu} \quad [1.509\times10^{-24}\ \mathrm{cm^2\ sr^{-1}\ keV^{-1}}], \tag{7}$$

where $Q = h\nu/E$ and $U = V/Z^2$; V is the accelerating voltage in esu. Coefficients a and b are

$$\begin{aligned} a &= 1.47B - 0.507A - 0.833, \\ b &= 1.70B - 1.090A - 0.627, \\ A &= \exp(-0.2230U) - \exp(-57.0U), \\ B &= \exp(-0.0828U) - \exp(-84.9U). \end{aligned} \tag{8}$$

The y-component, σ_y, is given as

$$\sigma_y = \frac{-\zeta + \eta/(Q+\varepsilon)}{Uh\nu} \quad [1.509\times10^{-24}\ \mathrm{cm^2\ sr^{-1}\ keV^{-1}}], \tag{9}$$

where

$$\begin{aligned} \zeta &= (1+2\varepsilon)y_2 - 2(1+\varepsilon)y_3, \\ \eta &= (1+\varepsilon)(y_3+\zeta), \\ \varepsilon &= \frac{-0.214y_1 + 1.21y_2 - y_3}{1.43y_1 - 2.43y_2 + y_3}, \\ y_1 &= 0.22[1 - 0.39\exp(-26.9U)], \\ y_2 &= 0.067 + 0.023/(U+0.75), \\ y_3 &= -0.00259 + 0.0076/(U+0.116). \end{aligned} \tag{10}$$

For $U < 0.0604$, the expressions modified by Statham [7]

$$\sigma_x = \exp(a_x)/h\nu \quad [1.509\times10^{-24}\ \mathrm{cm^2\ sr^{-1}\ keV^{-1}}], \tag{11}$$

$$\sigma_y = \exp(a_y)/h\nu \quad [1.509\times10^{-24}\ \mathrm{cm^2\ sr^{-1}\ keV^{-1}}], \tag{12}$$

are employed, where

$$a_x = (-1.019040 + 0.1460140Q - 0.0501077Q^2)\ln U - 1.483110 + 0.9474840Q - 0.350014Q^2,$$
$$a_y = (-0.882129 + 0.0366934Q - 0.339646Q^2)\ln U - 1.04088 - 1.86355Q - 0.723068Q^2. \quad (13)$$

The above analytical expressions are adopted in the range $0.2 < Q < 1$. For $Q < 0.2$, σ_x and σ_y are multiplied by the factors f_x and f_y, respectively, which are given as

$$f_x = 1 - 0.567\exp(-20Q)$$
$$f_y = \begin{cases} 1 & (\text{if } U > 0.0604) \\ 1 - (-0.55 + 4.83U)\exp(-20Q) & (\text{otherwise}). \end{cases} \quad (14)$$

The double differential bremsstrahlung cross section given by eq. (6) is depicted in Fig. 1 for X-rays of different photon energies under the condition that 10 kV electrons impinge on a Au atom. It can clearly be seen that the angular distribution of emitted X-rays is no longer homogeneous but is becoming an increasingly specified shape for higher photon energies.

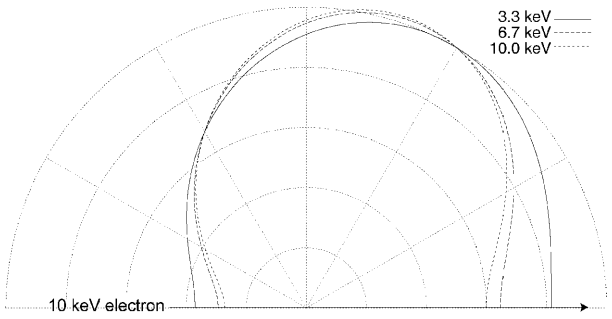

Fig. 1 Angular distributions of continuous X-rays of different photon energies emitted by interaction between a Au atom and 10 kV electrons.

2.3 Generation of characteristic X-rays

With respect to the generation of characteristic X-rays, the formula of Casnati [8] is used to calculate the ionization cross section of the *K* shell,

$$\sigma_K = n_K a_0^{\,2} R\left(\frac{I_0}{E_K}\right)^2 \psi\varphi\frac{\ln U}{U}, \quad (15)$$

where n_K is the number of electrons in the *K* shell, a_0 is the Bohr radius, E_K is the binding energy of the *K* shell, $U = E/E_K$ is the ratio of the electron kinetic energies *E* and E_K, and I_0 is the Rydberg constant.

The factor *R* is given by

$$R = \left(\frac{1+2J}{U+2J}\right)\left(\frac{U+J}{1+J}\right)^2 \times\left(\frac{(1+U)(U+2J)(1+J)^2}{J^2(1+2J)+U(U+2J)(1+J)^2}\right)^{\frac{3}{2}}, \quad (16)$$

where *J*, using the rest mass m_0, is

$$J = m_0c^2/E_K, \quad (17)$$

where *c* is the light velocity. Factors ψ and φ are

$$\psi = \left(\frac{E_K}{I_0}\right)^{(d_0+d_1/U+d_2/U^2)}, \quad (18)$$

$$\varphi = b_0\exp\left(\frac{b_1}{U}+\frac{b_2}{U^2}\right), \quad (19)$$

where $d_0 = -0.0318$, $d_1 = 0.316$, $d_2 = -0.1135$, $b_0 = 10.57$, $b_1 = -0.736$, and $b_2 = 0.317$.

Because the formula of Casnati is only applicable for the *K* shell, the ionization cross section of the *L* shell given by the conventional formula of Gryzinski [9] has been used. The ionization cross section of the *L* shell is obtained as

$$\sigma_L = n_L\frac{\sigma_0}{E_L^{\,2}}g(U), \quad (20)$$

where n_L is the number of electrons in the *L* shell, σ_0 and $g(U)$ are

$$\sigma_0 = 6.51\times10^{-14}\ [\text{eV}^2\,\text{cm}^2], \quad (21)$$

$$g(U) = \frac{1}{U}\left(\frac{U-1}{U+1}\right)^{\frac{2}{3}} \times\left\{1+\frac{2}{3}\left(1-\frac{1}{2U}\right)\ln[2.7+(U-1)^{\frac{1}{2}}]\right\}, \quad (22)$$

with E_L the binding energy of the L shell and $U = E/E_L$ the ratio of E_L to the electron kinetic energies E.

The method of calculation of the present Monte Carlo simulation has been described in detail elsewhere [10].

3. Effective resolution of phase-contrast image

In an X-ray microscope, a fine-focused electron beam bombards a thin film target to generate X-rays in the target to form an X-ray source of small size. The X-rays emitted from the X-ray source penetrate a sample placed beneath the target to project a shadow image onto a detector, e.g., film as schematically illustrated in Fig. 2.

The shadow image formed by absorption of the X-rays in the sample corresponds to the amplitude-contrast image in electron microscopy and should be distinguished from the phase-contrast image, which will be addressed below. As can easily be seen from the geometry, the spatial resolution d_a of the amplitude-contrast image is simply expressed by [11]

$$d_a = d_s(M-1), \tag{23}$$

where d_s is a source size and M the magnification [$=(a+b)/a$]. Eq. (23) clearly indicates that the resolution is wholly limited by the size of the X-ray source. With respect to the resolution of the phase-contrast image, we propose a simple model based on Fresnel diffraction for a point phase object, as described below.

Figure 3 is a schematic diagram of image formation in which we consider two paths of the X-rays emitted from a point source (S). One is the path of the X-rays diffracted by the point phase object at point (O) during penetration to attain the observation point (P); the other is the path of the X-rays that directly attain the point (P). The difference Δl between the two paths of the X-rays is given by

$$\begin{aligned}\Delta l &= (\overline{\mathrm{SO}} + \overline{\mathrm{OP}}) - \overline{\mathrm{SP}} \\ &= a + \sqrt{b^2 + x^2} - \sqrt{(a+b)^2 + x^2} \\ &\cong a + b\left(1 + \frac{x^2}{2b^2}\right) - (a+b)\left[1 + \frac{x^2}{2(a+b)^2}\right] \\ &= \frac{x^2}{2}\frac{a}{b(a+b)}.\end{aligned} \tag{24}$$

The first zero point (x_0) of the diffracted X-rays on the screen is simply attained for $\Delta l = \lambda/2$ as

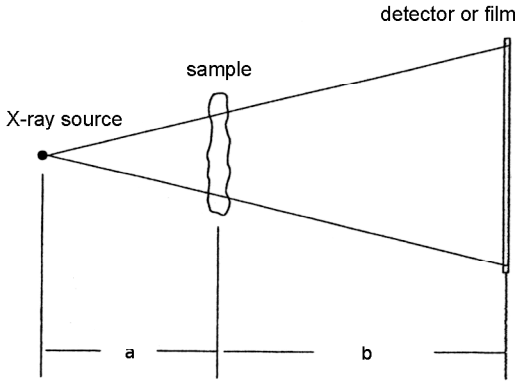

Fig. 2 Optics of X-ray radiography. *a*: distance between X-ray source and sample. *b*: distance between sample and film.

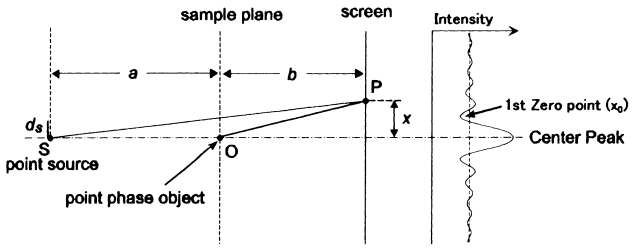

Fig. 3 Formation of Fresnel diffraction image of point phase object.

$$x_0 = \sqrt{\lambda\left[\frac{b}{a}(a+b)\right]} = \sqrt{\lambda b M}, \tag{25}$$

where $M = (a+b)/a$ is magnification of an object projected onto the screen by the point source.

Taking $2x_0$ as the diameter of the center peak of the Fresnel zone plate, the spatial resolution on the screen, Δd_{screen}, is given by

$$\Delta d_{screen} = 2\sqrt{\lambda b M}. \tag{26}$$

Converting the Δd_{screen} back to the object plane, one can get

$$\Delta d_{sample} = \frac{2}{M}\sqrt{\lambda b M} = 2\sqrt{\lambda \frac{ab}{a+b}}, \qquad (27)$$

by dividing Δd_{screen} with M.

It is this Δd_{sample} that basically determines the spatial resolution of X-ray phase-contrast microscopy. Dividing Δd_{screen} by b gives $\Delta\theta$, which is the angle of observing the center peak from the point phase object,

$$\Delta\theta = \frac{\Delta d_{screen}}{b} = 2\sqrt{\frac{\lambda M}{b}} = 2\sqrt{\lambda \frac{a+b}{ab}} = \frac{4\lambda}{\Delta d_{sample}}. \qquad (28)$$

Thus far, we have presumed a point source as an X-ray source and a practical source size has not been considered. Therefore, we will now try to extend the approach mentioned above to an X-ray source of finite size. Denoting the source size as d_s, the angle $\Delta\theta_s$, which sees the source from the point phase object, is given by

$$\Delta\theta_s = d_s / a. \qquad (29)$$

This angle is presumed to cause blurring of the Fresnel diffraction, leading to the ultimate blurred diffraction angle,

$$\Delta\theta_t = \sqrt{\Delta\theta^2 + \Delta\theta_s{}^2}. \qquad (30)$$

Hence, $\Delta\theta_t$ leads the diameter of the center peak converted to the object plane to

$$\Delta d'_{sample} = \Delta d_{sample}\frac{\Delta\theta_t}{\Delta\theta} = \Delta d_{sample}\sqrt{(\Delta\theta_s/\Delta\theta)^2 + 1}. \qquad (31)$$

Consequently, the d_s deteriorates the resolution Δd_{sample} for the point source by $\sqrt{(\Delta\theta_s/\Delta\theta)^2 + 1}$ times larger.

4. Results

4.1 X-ray microscopic observations

To explain the resolution of a phase-contrast image observed under an X-ray microscope, we studied two different observations. One was the X-ray microscopic image of an ant observed by one of authors (S. T.) in 1973 under irradiation of continuous X-rays from a Au film target 2 μm thick. The X-rays were generated in a Au (2 μm)/Mylar (2 μm)-film target by bombarding it with an electron beam of spot size ~2 μm in diameter at 10 kV and 0.38 μA. These arrangements were primarily aimed at making the source of the X-ray as small as possible. For this, a Au film target was selected for reducing the diffusion of incident electrons in the target, to make the X-ray source as small as possible. This also led us to use a low accelerating voltage such as 10 kV.

Figure 4 shows an X-ray microscopic image of an ant taken with Fuji FG film for electron microscopy at an exposure time of 30 min. The distances from the X-ray source to the object and from the object to the film were 5 mm and 50 mm, respectively.

The other image was of a bee observed by T. Kikuchi, also one of the authors, five years ago under irradiation of Cu-$K\alpha$ X-rays, generated in a Cu (20 μm) film target bombarded with an electron beam of 3 μm in diameter at 50 kV and 3 μA.

As described in Section 3, the spatial resolution of the phase-contrast image is restricted not only by the effective spot size of the X-ray source but also by the wavelength. In this case, it was aimed at using Cu-$K\alpha$ X-rays from a Cu foil target 20 μm thick. An electron beam of a higher accelerating voltage such as 50 kV was used to ensure an electron beam having a smaller spot size and high current intensity.

Figure 5 is the X-ray microscopic image of a bee taken with Fuji FG film at an exposure time of 20 min.

4.2 X-ray source sizes in film targets

The Monte Carlo simulation approach described in the preceding section was applied to evaluate the effective source sizes in the Au and Cu film targets under bombardment of 10 kV and 50 kV electrons, respectively.

The results are shown in Figs. 6 and 7. Figure 6 shows (a) the trajectories of 1000 incident electrons and (b) the spatial distribution of continuous X-rays generated in the Au (2 μm) film target under bombardment of 10 kV electrons at normal incidence, which simulates the X-ray microscopic observation of the ant shown in Fig. 4. Similarly, Fig. 7 shows (a) the trajectories of 1000 incident electrons and (b) the spatial distribution of Cu-$K\alpha$ X-rays generated in the Cu (20 μm) film target, under bombardment of 50 kV electrons at normal incidence, which simulates the other X-ray microscopic observation of the bee shown in Fig. 5.

From these results, effective source sizes of signal X-rays were evaluated by plotting the lateral distribution of X-ray intensity, as seen in Fig. 8. The Monte Carlo calculations were performed for an electron beam of a definite spot size

Fig. 4 X-ray microscopic image of an ant. X-ray power, 10 kV × 0.38 μA; electron beam spot, 2 μm in diameter; exposure time, 30 min with Fuji FG film for transmission electron microscopy; X-ray source (Au film target 2 μm thick) to sample, 5 mm; sample to film, 50 mm.

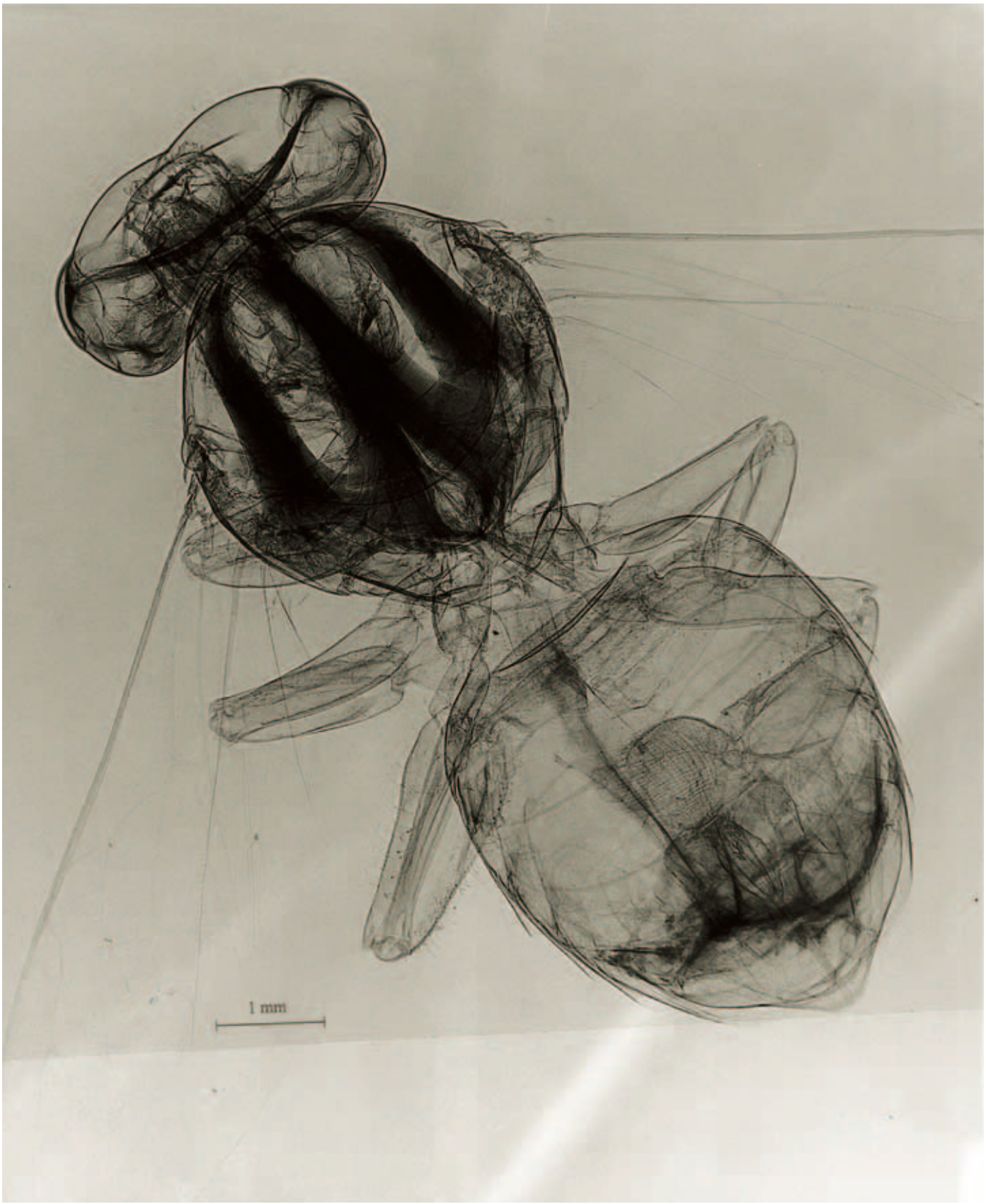

Fig. 5 X-ray microscopic image of a bee. X-ray power, 50 kV × 3 μA; electron beam spot, 3 μm in diameter; exposure time, 20 min with Fuji FG film. X-ray source (Cu film target 50 μm thick) to sample, 100 mm; sample to film, 200 mm.

according to the experiment, namely, a 10-kV electron beam of 2 μm in diameter for the Au film target and a 50-kV electron beam of 3 μm in diameter for the Cu foil target.

The lateral distribution of the X-ray intensity in the Au film target is plotted in Fig. 8 for X-rays of photon energies higher than 5 keV because a major part of the X-rays of photon energies below 5 keV is absorbed in the target, as seen in Fig. 9. As is clearly shown in Fig. 8, the effective source of the X-rays in the Au target is fully determined by the electron beam size, i.e., ~2 μm in diameter in this case.

The other lateral distribution of Cu-$K\alpha$ X-ray intensity in the Cu (20 μm) film target is plotted in Fig. 10. The effective source size in the Cu foil target becomes considerably larger than the spot size of the electron beam owing to the diffusion of the incident electrons in the target. The X-ray source size in the Au target is almost the same as the spot size of the electron beam. Here, the diffusion of 10 kV electrons in the Au target is one order of magnitude smaller than the spot size of the electron beam.

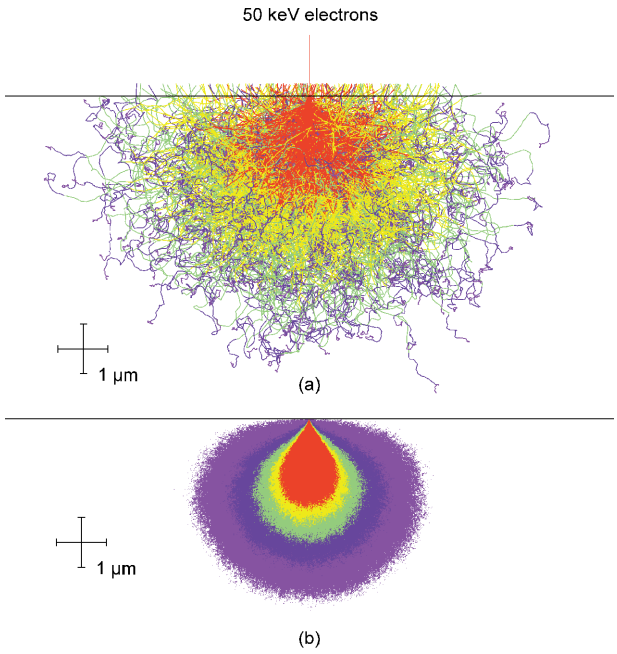

Fig. 7 (a) Trajectories of incident 50 kV electrons in Cu-target, demonstrating the deceleration process by color : Red, 50-40 keV ; yellow, 40-30 keV ; green, 30-20 keV ; blue, 20-10 keV ; purple, 10-0 keV. (b) Spacial distribution of Cu-$K\alpha$ X-rays generated in the Cu-target. The colored area represent those of different photon densities [photons/(μm^2 · electron)]of Cu-$K\alpha$ X-rays : Red, > 1.0 × 10^{-3} ; yellow, > 0.8 × 10^{-3} ; green, > 0.6 × 10^{-3} ; blue, > 0.4 × 10^{-3} ; purple, > 0.2 × 10^{-3}.

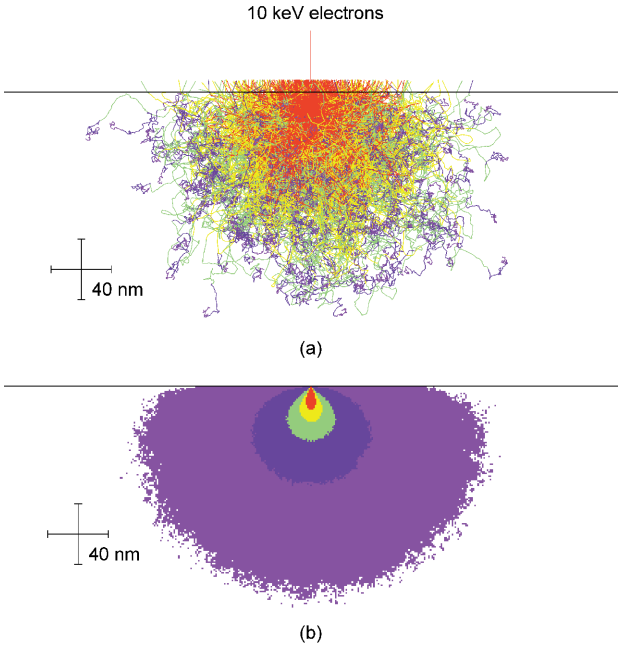

Fig. 6 (a) Trajectories of incident 10 kV electrons in Au target and (b) spatial distribution of X-rays of different photon energies generated in the Au target. Purple, 0-2 keV ; blue, 2-4 keV ; green, 4-6 keV ; yellow, 6-8 keV ; and red, 8-10 keV.

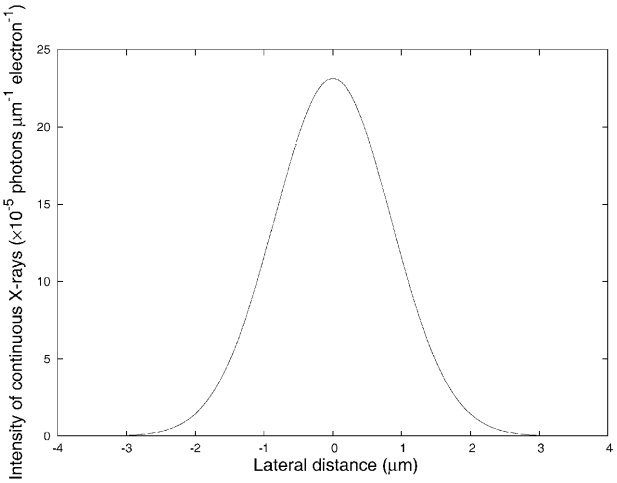

Fig. 8 Lateral distribution of continuous X-rays of photon energies higher than 5 keV generated in Au target under bombardment of 10-kV electron beam of 2 μm diameter at normal incidence.

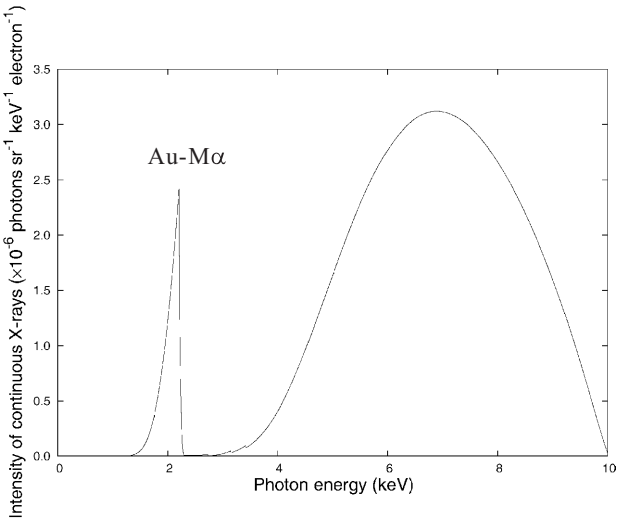

Fig. 9 Spectrum of continuous X-rays emitted from Au target under bombardment of 10-kV electrons at normal incidence.

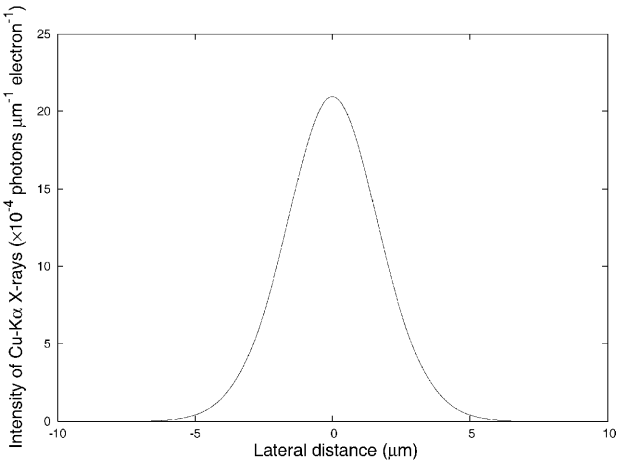

Fig. 10 Lateral distribution of Cu-$K\alpha$ X-rays in Cu target under bombardment of 50-kV electron beam 3 μm in diameter at normal incidence.

5. Discussion

5.1 Phase-contrast image of an ant

Let us examine the spatial resolution of the image shown in Fig. 4. In this case, the distances from the X-ray source to the object (ant) and the object to the film (screen) are 5 mm and 50 mm, respectively, that is, $a = 5$ mm and $b = 50$ mm. Thus, the magnification is calculated as

$$M = (a+b)/a = 11.$$

According to the X-ray spectrum emitted from the Au target shown in Fig. 9, in this case we presumed $\overline{\lambda} = 1.8$ Å as an average wavelength of the continuous X-rays. First, for the point source of X-rays we get

$$\Delta d_{screen} = 2\sqrt{\overline{\lambda} bM} \cong 20\ \mu\text{m},$$
$$\Delta d_{sample} = \frac{\Delta d_{screen}}{M} \cong 1.8\ \mu\text{m},$$

and

$$\Delta\theta = 2\sqrt{\overline{\lambda}\,\frac{a+b}{ab}} \cong 4.0\times10^{-4}\ \text{rad}.$$

With respect to the definite source size of the X-rays, taking the effective source size, d_s, in the present case, as $d_s = 2$ μm, we get

$$\Delta\theta_s = \frac{2\ \mu\text{m}}{5\ \text{mm}} = 4\times10^{-4}\ \text{rad},$$
$$\therefore \frac{\Delta\theta_t}{\Delta\theta} = \frac{\sqrt{\Delta\theta^2 + \Delta\theta_s^{\,2}}}{\Delta\theta} \cong 1.4.$$

Therefore, the ultimate resolution $\Delta d'_{sample}$, is given by

$$\Delta d'_{sample} = \Delta d_{sample} \times 1.4 \cong 2.6\ \mu\text{m},$$

and

$$\Delta d'_{screen} = \Delta d_{screen} \times 1.4 \cong 28\ \mu\text{m}.$$

This value of $\Delta d'_{screen}$ should be larger than the resolving power of the detector, Δd_0. This requirement is satisfied in this case because the resolving power of the Fuji FG film is regarded as $\Delta d_0 \cong 15$ μm.

A careful examination of Fig. 4 reveals that the resolution attains 2~3 μm, agreeing well with the evaluation mentioned above.

It is worth noting that the ultimate resolution of the phase-contrast image comes very close to the source size of the X-

rays, much higher than the resolution of the amplitude-contrast (absorption) image which is, according to eq. (23), estimated as $d_0 \cong 20$ μm.

Another point of practical importance is that a dark line is associated with an adjacent bright line or vice versa. This is a feature of the diffraction pattern often observed in Kossel and Kikuchi patterns. This line pair of bright and dark lines leads to the effect of emphasizing line and edge contrasts just as in differentiated image processing, which is commonly used for emphasizing image contrast.

Consequently, the phase-contrast images observed in X-ray microscopy increase not only higher spatial resolution but also higher contrast.

5.2 Phase-contrast image of a bee

Applying the same approach as mentioned in Section 5.1 to the phase-contrast image of a bee, shown in Fig. 5, we have obtained the ultimate effective resolution as follows:

First, taking $a = 100$ mm, $b = 200$ mm, and $\lambda = 1.542$ Å (Cu-$K\alpha$ X-rays), we get

$$\Delta d_{screen} = 2\sqrt{\lambda bM} \cong 19 \text{ μm},$$
$$\Delta d_{sample} = \frac{\Delta d_{screen}}{M} \cong 6.4 \text{ μm},$$

and

$$\Delta\theta = 2\sqrt{\lambda \frac{a+b}{ab}} \cong 9.6\times10^{-5} \text{ rad}.$$

Presuming that the effective source size $d_s = 3.9$ μm, we get

$$\Delta\theta_s = \frac{3.9 \text{ μm}}{100 \text{ mm}} = 3.9\times10^{-5} \text{ rad},$$
$$\Delta\theta_t = \sqrt{\Delta\theta^2 + \Delta\theta_s{}^2} \cong 10\times10^{-5} \text{ rad}.$$

Therefore, the effective resolution is given by

$$\Delta d'_{sample} = \Delta d_{sample} \frac{\Delta\theta_t}{\Delta\theta} \cong 6.9 \text{ μm}.$$

In this case, the reason why the resolution of the phase-contrast image becomes almost twice as large as the X-ray source size is mostly due to the experimental setup, namely the smaller value of M, as suggested by

$$\Delta d_{sample} = 2\sqrt{\lambda b / M}.$$

If one had chosen, for instance, $a = 10$ mm and $b = 200$ mm, one would have obtained a much higher resolution as

$$\Delta d'_{sample} \cong 4.4 \text{ μm},$$

which is much better than the resolution obtained in the experiment. Furthermore, also note that the ultimate resolution $\Delta d'_{sample}$ again comes very close to the source size whereas the resolution of the amplitude-contrast image is predicted from eq. (23) to be twice as large as the source size.

6. Summary

The present paper has proposed a simple equation (eq. (31)) to evaluate the effective resolution of phase-contrast images observed under an X-ray microscope and demonstrated its usefulness by applying it to two X-ray microscopic observations. The results are summarized as follows:

(1) Particular attention was drawn to the two features of phase-contrast images: One is that much higher spatial resolution is attainable than that of the conventional amplitude-contrast (absorption) image. The other is line-pair contrast, in which a dark line is always associated with an adjacent bright line or vice versa. This line-pair contrast leads to the effect of emphasizing line and edge contrast just as does differentiated image processing, which is commonly used for emphasizing image contrast.

(2) The effective source sizes of X-rays are evaluated by applying Monte Carlo simulation, the source program of which has recently been rewritten in C++ for more practical use.

(3) Monte Carlo calculations provided the effective X-ray sources, 2 μm in diameter for Au (2 μm) / Mylar (2 μm)-film target under bombardment of an electron beam ~2 μm in diameter, 10 keV, and 0.38 μA.

(4) Similarly, the effective source size of Cu-$K\alpha$ X-rays was evaluated to be ~3.9 μm in diameter in a Cu foil (20 μm) target under bombardment of an electron beam of ~3 μm in diameter, 50 keV, and 3 μA.

(5) Eq. (31) predicted that the resolutions of the two phase contrast images (shown in Figs. 4 and 5) attain ~2.6 μm for Fig. 4 and ~6.9 μm for Fig. 5, which describe the observations with considerable success.

(6) Eq. (31) also suggests that the resolution in Fig. 5 should be greatly improved by a different setup of the experiment, such as setting $a = 10$ mm in place of $a = 100$ mm in the original observation. This new setup is predicted to provide the ultimate resolution of ~4.4 μm, much better than ~6.9 μm in the original observation.

Acknowledgment

The authors are very grateful to Professor (Emeritus) Jinpei Harada, for drawing our attention to the phase-contrast image observed under an X-ray projection microscope. This led them to performing the joint work presented in this paper.

References

[1] M. v. Ardenne, Elektronen-übermikroskopie, Springer-Verlag, Berlin (1940).

[2] S. W. Wilkins, T. E. Gureyev, D. Gao, A. Pogany and A. W. Stevenson, *Nature*, **384**, 335 (1996).

[3] J. Henoc and F. Maurice, in Quantitative Electron Probe Microanalysis, NBS-Special Publ. Vol. 298, ed. by K. F. J. Heinrich, pp. 61~70, NBS, Gaithersburg, MD (1968).

[4] R. D. Birkhoff, in Handbuch der Physik, Band XXXIV, ed. by S. Flügge, pp. 53~138, Springer-Verlag, Heidelberg (1958).

[5] M. J. Berger and S. M. Seltzer, Studies in Penetration of Charged Particles in Matter, Natl. Acad. Sci. Publ. Vol. 1133, pp. 205~268, Natl. Acad. Sci., Washington, D.C. (1964).

[6] P. Kirkpatrick and L. Wiedmann, *Phys. Rev*., **67**, 321 (1945).

[7] P. J. Statham, *X-ray spectrum*, **5**, 154 (1976).

[8] E. Casnati, A. Tartari and C. Baraldi, *J. Phys*. B, **15**, 155 (1982).

[9] M. Gryzinski, *Phys. Rev*., **138**, 336 (1965).

[10] Y. Yamaguchi and R. Shimizu, *Surf. Interface Anal*., **38**, (2006) in press.

[11] P. Kirkpatrick and H. H. Pattee, in Handbuch der Physik, Band XXX, ed. by S. Flügge, pp. 305~336, Springer-Verlag, Heidelberg (1957).